



ARTICLE

Open Access

Role and dynamics of vacuolar pH during cell-in-cell mediated death

Yan Su^{1,2}, He Ren^{2,3}, Meng Tang^{2,3}, You Zheng², Bo Zhang^{2,3}, Chenxi Wang², Xinyu Hou³, Zubiao Niu², Zhongyi Wang², Xiaoyan Gao^{2,3}, Lihua Gao², Hong Jiang⁴, Zhaolie Chen², Tianzhi Luo¹  and Qiang Sun¹ 

Abstract

The nonautonomous cell death by entosis was mediated by the so-called cell-in-cell structures, which were believed to kill the internalized cells by a mechanism dependent on acidified lysosomes. However, the precise values and roles of pH critical for the death of the internalized cells remained undetermined yet. We creatively employed keima, a fluorescent protein that displays different excitation spectra in responding to pH changes, to monitor the pH dynamics of the entotic vacuoles during cell-in-cell mediated death. We found that different cells varied in their basal intracellular pH, and the pH was relatively stable for entotic vacuoles containing live cells, but sharply dropped to a narrow range along with the inner cell death. In contrast, the lipidation of entotic vacuoles by LC3 displayed previously underappreciated complex patterns associated with entotic and apoptotic death, respectively. The pH decline seemed to play distinct roles in the two types of inner cell deaths, where apoptosis is preceded with moderate pH decline while a profound pH decline is likely to be determinate for entotic death. Whereas the cancer cells seemed to be lesser tolerant to acidified environments than noncancerous cells, manipulating vacuolar pH could effectively control inner cell fates and switch the ways whereby inner cell die. Together, this study demonstrated for the first time the pH dynamics of entotic vacuoles that dictate the fates of internalized cells, providing a rationale for tuning cellular pH as a potential way to treat cell-in-cell associated diseases such as cancer.

Introduction

Cell-in-cell structure (CICs) refers to a unique type of cellular structure characterized by the enclosure of one or more cells into the cytosolic vacuoles of another cell. CICs had been mostly documented in various of human tumors^{1,2}, such as pancreatic cancer^{3,4}, head and neck squamous cell carcinoma^{5,6}, and breast cancer^{7,8}, where it was proposed to mediate competition between tumor cells to facilitate clonal selection and tumor evolution⁹. Meanwhile, recent studies implicated CICs in a wider range of biological processes, such as embryonic development¹⁰, genome stability^{11,12}, virus infection^{13,14}, and

immune homeostasis^{15,16} and the like. Over the past decade, intensive efforts were endeavored to decipher the molecular mechanisms underlying the formation of CICs, among which entosis represents one of the mostly studied programs. During entotic CIC formation, the polarized adherens junction and contractile actomyosin are two well-established core elements^{17,18}. Recently, the vinculin-enriched mechanical ring was identified as a novel core element interfacing between adherens junction and actomyosin to coordinate cell internalization¹⁹. Besides, a group of factors, by acting on the core elements, were identified to regulate CIC formation, such as PCDH7, CDKN2A, MTRF, and LPA and the like^{20–25}.

Despite of the great progress made on the formation mechanisms for CICs, much less is known about the fate control of the internalized cell in CICs. It was proposed that entosis was a CICs-mediated type IV programmed death²⁶, which resulted in lysosomal entotic death as a predominant mechanism and apoptotic death as an

Correspondence: Tianzhi Luo (tluo@ustc.edu) or Qiang Sun (sunq@bmi.ac.cn)

¹CAS Key Laboratory of Mechanical Behavior and Design of Materials, Department of Modern Mechanics, University of Science and Technology of China, Hefei, China

²Laboratory of Cell Engineering, Institute of Biotechnology, Beijing, China

Full list of author information is available at the end of the article

These authors contributed equally: Yan Su, He Ren

Edited by L. Sun

© The Author(s) 2021



Open Access This article is licensed under a Creative Commons Attribution 4.0 International License, which permits use, sharing, adaptation, distribution and reproduction in any medium or format, as long as you give appropriate credit to the original author(s) and the source, provide a link to the Creative Commons license, and indicate if changes were made. The images or other third party material in this article are included in the article's Creative Commons license, unless indicated otherwise in a credit line to the material. If material is not included in the article's Creative Commons license and your intended use is not permitted by statutory regulation or exceeds the permitted use, you will need to obtain permission directly from the copyright holder. To view a copy of this license, visit <http://creativecommons.org/licenses/by/4.0/>.

alternate program when lysosomal function was disrupted²⁷. The LC3 lipidation onto the entotic vacuole seemed to be associated with the death of the internalized cells via facilitating its fusion with adjacent small lysosomes²⁸. The dead inner cells were cleared by entotic vacuoles, as a huge lysosome actually, through active fusion and fission processes^{29,30}. This process was shown to be tightly regulated by a mTORC1-dependent pathway that redistributes degraded cargo back into the endosomal network²⁹, and a PIKfyve-dependent pathway that controls vacuole shrinkage and nutrient recovery partially through the lysosomal cation channel TRPML1/MCOLN1³⁰. Nevertheless, previous studies of the death mechanisms of the internalized cells had not dealt with the critical condition of lysosome acidification for cell death and degradation, and the determined turning point for the fates of internalized cells.

We here introduced keima^{31,32}, a protein pH sensor, to measure the precise pH of entotic vacuoles during the death of internalized cells and explore the complementary relationship between entotic death and apoptotic death. Keima is a coral-derived acid-stable fluorescent protein that has a bimodal excitation spectrum peaking at 440 and 550 nm corresponding to the neutral and ionized states³². Generally, the dual-excitation ratio (550 nm/440 nm) of this probe can precisely indicate the cellular pH value, allowing its extensive usage in various studies of cell physiology. Keima was adopted to detect autophagic events based on lysosomal delivery³³, and was also applied as a marker of mitophagy³⁴ to explore autophagosome-lysosome fusion³⁵. With this genetically encoded fluorescent protein, we could conveniently probe the pH dynamics of cell death occurring within CICs.

In this study, we studied the pH titration behaviors of keima-overexpressed cells using gradient pH buffer, which enabled us to readout the context-specific pH value for each cell lines based on its correlation with the dual-excitation ratios of keima protein. The keima-overexpressed cells were then applied to the time-lapse assay to measure the accurate pH value of entotic vacuole during the process of the inner cell death associated with different patterns of LC3 lipidation. Moreover, we demonstrated that manipulating lysosomal acidification is effective in controlling inner cell fates as well as the ways whereby the inner cells die.

Materials and methods

Antibodies and chemical reagents

The following antibodies were used: anti-cleaved-caspase 3 (1:200; CST, #9664s) and secondary Alexa Fluor 647 anti-rabbit (1:500; Invitrogen, #A-20991). Reagents including EN6 (Selleck, #S6650), Hydroxychloroquine (CQ) (MCE, #HY-W031727), Concanamycin A (ConA) (Shanghai ZZbio.co, ZAE-ALX-380-034-C025),

NH4Cl (Coolaber, CA30112320), LysoTracker (Invitrogen, #L7526), DAPI (Life technologies, #D1306) were purchased and used according to manufacturer's instructions.

Cells and culture conditions

Cell lines MCF7, SW480 expressing E-cadherin (SW480/E), MDA-MB-231 expressing E-cadherin (MDA-MB-231/E), HEK293T, and their derivatives were cultured in Dulbecco's modified Eagle's medium (MACGENE Technology Ltd., Beijing, China) supplemented with 10% fetal bovine serum (Kangyuan Biology, China). MCF10A and their derivatives were maintained in DMEM/F12 (Gibco, USA) supplemented with 5% equine serum (Kangyuan Biology, China), 20 ng/ml EGF (Peprotech, USA), 10 g/ml insulin (Sigma, USA), 0.5 ug/ml hydrocortisone (Sigma, USA), and 100 ng/ml cholera toxin (Sigma, USA). All cells were cultured in the humidified incubator of 5% CO₂ at 37 °C.

Cloning and generation of stable cell lines

pQCXIP-mKeima-N1 was cloned by inserting the mKeima sequence (pCHAC-mt-mKeima, Addgene, #72342) into *Bam*H I/*Sal* I sites of the pQCXIP-N1 vector using the T4 DNA ligase (New England BioLabs, #M0202S) according to manufacturer's instructions. The cDNA encoding EGFP-LC3 fusion protein was released from pBABE-EGFP-LC3-puro (Addgene, #22405) and cloned into pQCXIN-EGFP-N1-Neo by the 5'-*Eco*R I and 3'-*Age* I sites. To generate stable cell lines, retroviruses were packaged in HEK293T cells using Lipofectamine 2000 reagent (Invitrogen) as described before³⁶. All cell lines were transduced with viruses for 24 h with 8 µg/ml polybrene (Sigma). Virus-infected cells were selected and grown in medium with 2 µg/ml puromycin or 200 µg/ml G418.

RNA interference

For siRNA transfection, cells (2×10^5 /well) were plated into a 12-well plate and cultured overnight, then transfected with 50 nM siRNA (GenPharma, China) using Lipofectamine RNAiMAX (Invitrogen, #13778-150). siRNA sequence: siATG5-1: 5'-AGATTGAAGGATCAA CTATTT-3'; siATG5-2: 5'-CCTGAACAGAATCATCC TTAA-3'; siATG7-1: 5'-GCCTGCTGAGGAGCTCTCC AT-3'; siATG7-2: 5'-GGCGTGAGACACATCACATTT-3'; siATP6V0A2: 5'-CGTAAGTTCTTTCCAAAGAAA-3'; siATP6V1A: 5'-CCTACGGTTGGTAGTCATAT-3'; Negative Control: 5'-UCUCCGAACGUGUC ACGUTT-3'.

Reverse transcription-quantitative PCR (RT-qPCR)

Total RNA was isolated from cells 48 h after siRNA transfection using TRIzol reagent (Invitrogen, #15596026) and converted into cDNA using TransScript One-Step gDNA Removal and cDNA Synthesis SuperMix

(Transgen Biotech, #AT311-02). The cDNA was used to perform qPCR by SYBR Green Real-time PCR Master Mix (TOYOBO, #QPK-201). Fold changes were calculated using the $2^{-\Delta\Delta C_t}$ method and were expressed as means \pm SD of triplicate quantification. The following primer pairs were used: ATG5: 5'-GCTATTGATCCTGAAGATGGG-3' and 5'-GATGTTCACTCAGCCACTG-3'; ATG7: 5'-GTTGACCCAGAAGAAGCTG-3' and 5'-CAGAGTCAC CATTGTAGTAATAACC-3'; ATP6V0A2: 5'-GGATCT CTACACTGTACTGCA-3' and 5'-CAGAGCATGAAGA GAAGTTCC-3'; ATP6V1A: 5'-GAGGAGTAAACGTGT CTGC-3' and 5'-TATGACTACCAACCCGTAGG-3'; GAPDH: 5'-ACAACCTTTGGTATCGTGGAAGG-3' and 5'-GCCATCACGCCACAGTTTC-3'.

pH titration

Cells overexpressing fluorescent protein keima were incubated in a series of buffers with pH values ranging from 4.12 to 7.97, then the fluorescent signal of keima was measured under the conditions of excitation of 440 and 550 nm and emission of 610 nm using Nikon ECLIPSE Ti-U epi-fluorescence microscope. Then the fluorescent intensity of keima was measured by NIS-Elements F 3.0 software³⁷. The pH titration curves and fitting equation were obtained by the negative correlation between the pH value and the fluorescent intensity ratio of 550 nm/440 nm of keima protein.

Time-lapse microscopy

Cell-in-cell time-lapse assay was performed as previously described². About 3×10^5 cells were suspended in 0.5% agarose-coated plates for 6 h, and then cell suspensions were transferred and grown on cover-glass dishes. Images of cells were captured for DIC and fluorescence channels (excitation of 440 and 550 nm and emission of 610 nm) every 10 min with $\times 20$ objective lenses at 37 °C and 5% CO₂ for 24 h by the Nikon ECLIPSE Ti-U epi-fluorescence microscope and analyzed by NIS-Elements F 3.0 software (Nikon, Japan). The timing of cell death was judged morphologically by the appearance of a broken cell membrane, or cessation of cell movement, or both.

LysoTracker staining

LysoTracker staining was performed according to manufacturer's instructions. LysoTracker FITC (Invitrogen, #L7526) dissolved in serum-free medium was added to keima-expressing cells for 30 min at 37 °C. After that, cells were washed with PBS and cultured in complete growth medium followed by imaging using Nikon ECLIPSE Ti-U epi-fluorescence microscope.

Immunostaining

Immunostaining was performed as previously described³⁸. Briefly, cells were fixed in 4% paraformaldehyde for

10 min at room temperature, then permeabilized with 0.2% Triton X-100/PBS for 3 min and washed with PBS followed by blocking with 5% BSA at room temperature for 1 h. Fixed samples were incubated with primary antibody at 4 °C overnight and washed with PBS before incubated with fluorophore-labeled secondary antibodies at room temperature for 1 h. Cells mounted with mounting medium with DAPI (ZSGB-BIO, #ZLI-9557) and imaged by Nikon ECLIPSE Ti-U epi-fluorescence microscope.

Statistical analysis

All of the experiments were performed for at least three times. Data were displayed as mean \pm SD. *p* values were calculated by two-tailed Student's *t* test or Dunnett *t* test using Excel or GraphPad Prism software, with statistical significance assumed at *p* < 0.05.

Results

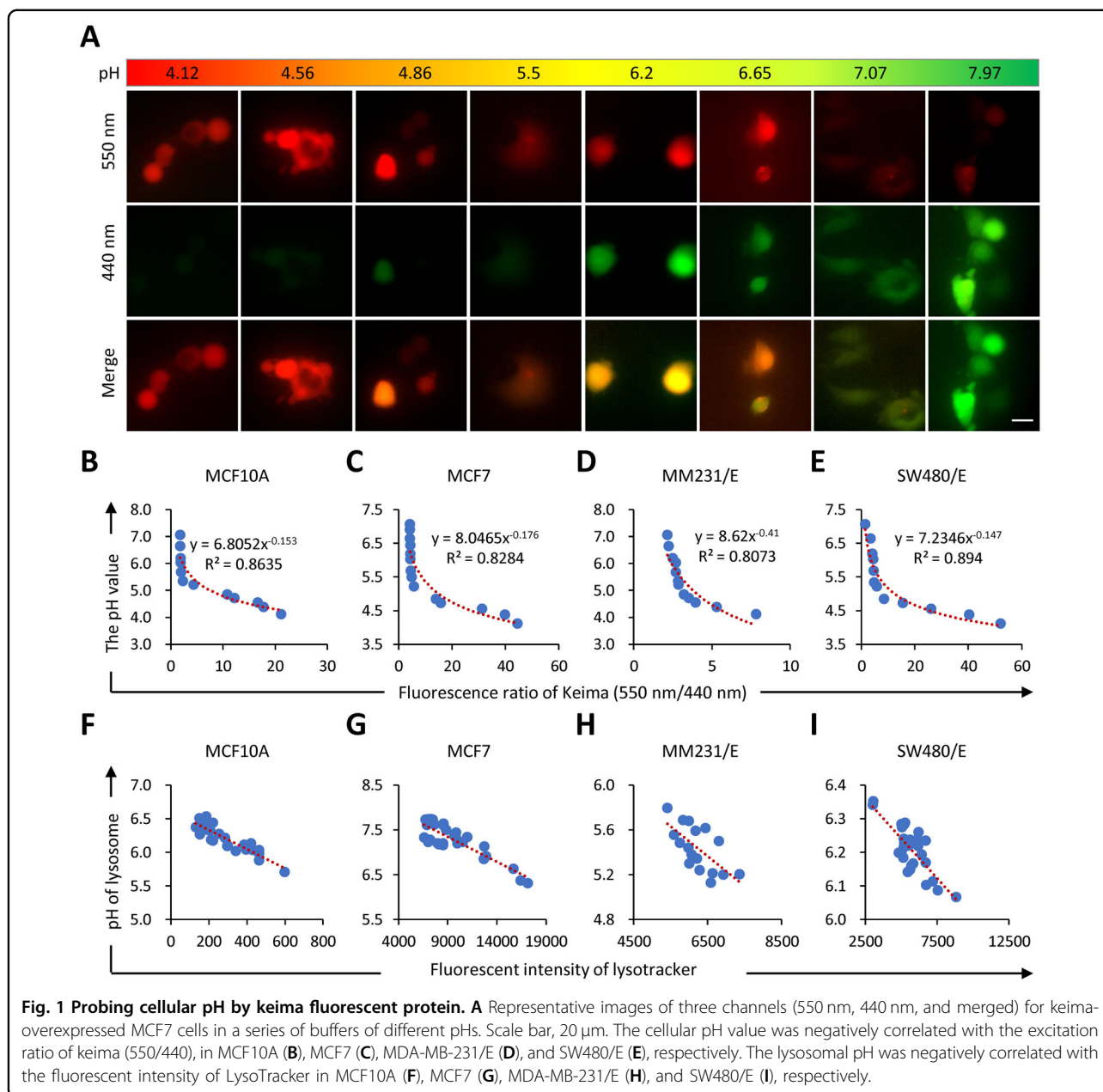
Keima-based monitoring of the cellular and lysosomal pH values

To monitor the pH dynamics in live cells, we made cell lines that stably expressed keima, a genetically engineered protein pH meter that displays different excitation spectra upon pH changes. As shown in Fig. 1A, the excitation at 550 nm decrease accompanied with an increase in excitation at 440 nm when the buffering pH is getting higher, which is consistent with the published study³³. Briefly, keima displayed red in the acidified buffer (pH 4.12–5.5), green in the neutral buffer (pH 7.07–7.97), and orange in the transitory buffer (pH 5.6–7.06). For accurate pH measurement based on keima excitation, we managed to make a correlation between the pH value and the ratio of keima excitations (550 nm/440 nm), and obtained pH titration curves for four entosis-proficient cell lines: MCF7, MCF10A, SW480 expressing E-cadherin (SW480/E), and MDA-MB-231 expressing E-cadherin (MM231/E), respectively (Fig. 1B–E). Interestingly, based on the titration curves and the derived equations, the above four cell lines were found to have profoundly different intracellular pH values (Fig. S1B, C).

In agreement with its pH-sensitive property, keima displayed bright red fluorescent signals (550 nm) at the subcellular regions marked by lysotracker, a fluorescent dye specifically labeling lysosomes (Fig. S1A)³⁹. Remarkably, the pH values derived from the keima ratio of 550 nm/440 nm were tightly correlated with the intensity of lysotracker at the subcellular organelle of lysosomes (Fig. 1F–I), further supporting the liability of keima to be an in situ pH meter for live cell analysis.

The pH dynamics during the death of internalized cells

By taking advantage of the keima-expressing cells as a pH readout, we firstly tried to examine the pH changes of



the entotic vacuoles during the inner cell death of MCF10A cells. As shown in Fig. 2A, the entotic vacuoles gradually turned into yellow and subsequently into red along with the death and degradation of the inner cells, indicating progressive vacuolar acidification (Fig. S3A and Movie S1). Based on the changes in keima excitation and inner cell morphology, the death process could be roughly divided into four steps, including internalization (S1), acidification (S2), entotic death (S3), and degradation (S4) (Fig. 2B). While the pH changed little in the outer cells, it kept declining in the dying inner cells during the four sequential stages (S1–S4) (Fig. 2B, C). By contrast, the live inner cells were in green throughout the whole process of

time-lapse imaging (Fig. S3B and Movie S2), which is similar to those of the outer cells and non-CICs live cells (Fig. S3C), indicating relative stable pH of the entotic vacuoles containing live cells.

For the sake of more accurate evaluation, we calculated the rate of the pH changes in different categories of cells, and found that the pH of vacuoles with dying cells decreased at a speed of 0.0678–0.1779 per h that was significantly faster than those for vacuoles with live cells (–0.0236 to 0.0632 per h) (Fig. 2D). The mean pH of the non-CIC normal cells (6.14) was slightly higher than that of the alive inner cells (5.74) which was significantly higher than that of dead inner cells (4.90) (Fig. 2E).

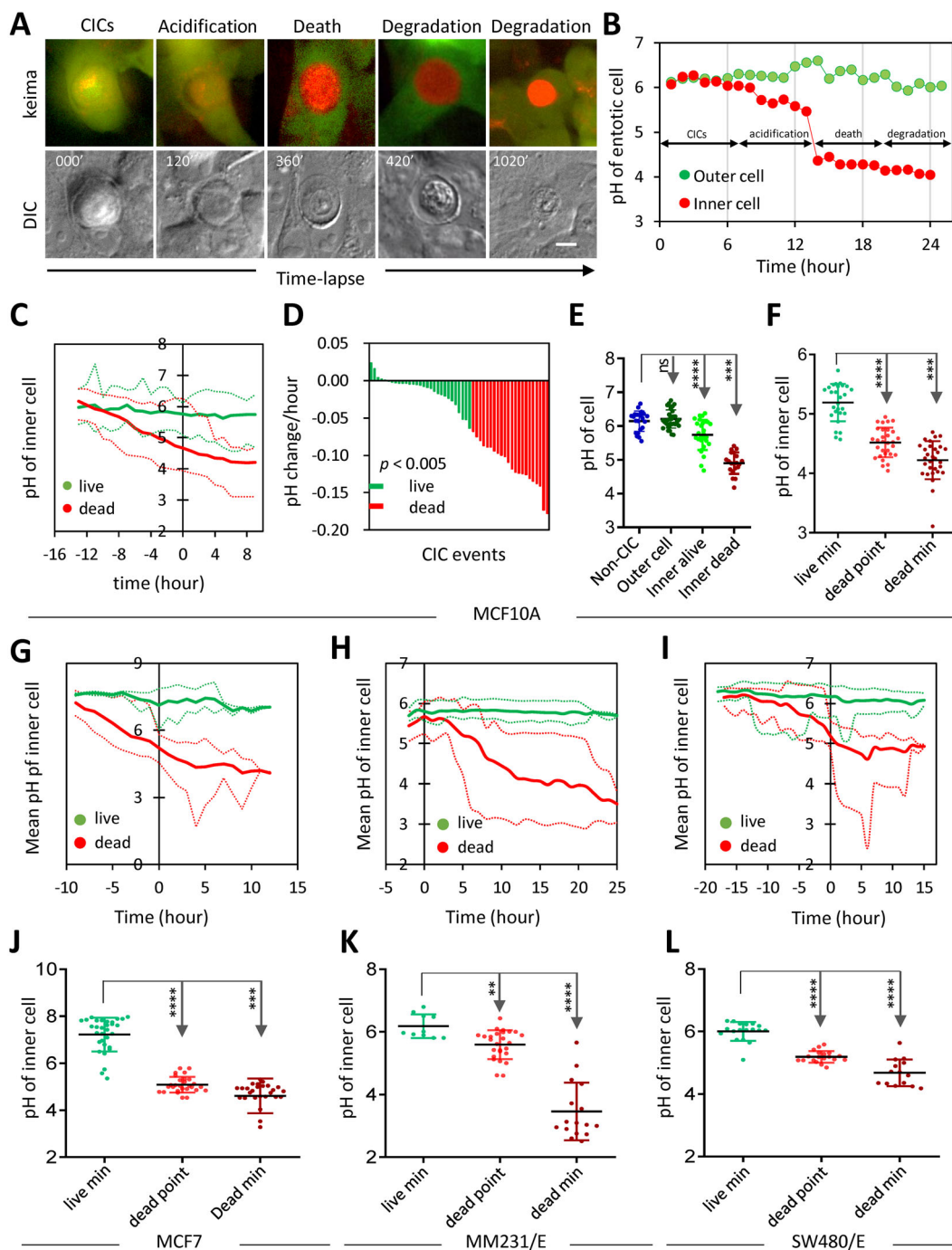


Fig. 2 The pH dynamics during the CICs-mediated death. **A** The time-lapse images showed keima signal changes in one CICs from MCF10A cells. The keima channel was merged from 440 nm (green) and 550 nm (red) channels. Scale bar, 10 μ m. **B** The quantitative presentation of pH changes in **A** for the respective inner and outer cell over time course. **C** The pH changes of inner cells from a group of CICs over time. The solid lines are for the mean pH while the upper dotted lines and lower dotted lines indicate the pH ranges. The inner cell death was set as time zero. $n = 17$ (dead), 28 (live). **D** The change of pH value per hour for live (green) and dead inner cells (red), respectively. **E** Quantification of the cellular pH for non-CIC cells (blue), outer cells (dark green), live inner cells (green dots), and dead inner cell (dark red). **F** Graph shows the minimum pH of live inner cell (green), the pH of dead inner cells at the moment of cell death (bright red) and minimum pH of the dead inner cell (dark red). The pH of inner cells changed over time in the keima-overexpressed MCF7 (**G**), MDA-MB-231/E (**H**), and SW480/E (**I**), respectively. **G** $n = 12$ (dead), 8 (live); **H** $n = 12$ (dead), 17 (live); **I** $n = 19$ (dead), 18 (live). **J-L** Graph shows the minimum pH of live inner cell (green), the pH of dead inner cells at the moment of cell death (bright red) and minimum pH of the dead inner cell (dark red) for MCF7 (**G**), MDA-MB-231/E (**H**), and SW480/E (**L**), respectively. $**p < 0.01$; $***p < 0.001$; $****p < 0.0001$.

Importantly, the pH of 4.5 seemed to be the dead point, referring to dead pH hereafter, for the internalized MCF10A cells as no cells were found to be alive at pH below 4.5, whereas cells would be alive within vacuoles of pH >5.0 (Fig. 2F). Similar dynamics were obtained on the other three entosis-proficient cells (Fig. 2G–I). However, the dead pH varied with 5.0 for MCF7 cells (Fig. 2J), 5.6 for MDA-MB-231/E cells (Figs. 2K and S3D, E), and 5.2 for SW480/E cells (Figs. 2L and S3F, G). Interestingly, the dead pHs for the later three cells that are cancer cells were much higher than that of MCF10A cells that are non-transformed epithelial cells (Fig. 2F, J–L). These data suggest that the vacuolar pH is critical for the fate control of the internalized cells, which, however, is context-dependent, and cancer cells seemed to be less tolerant to the acidified environments than the noncancerous epithelial cells.

LC3 lipidation onto the entotic vacuoles in complex patterns

LC3 lipidation of the entotic vacuole was reported to be a critical event taking place right prior to and mediating entotic cell death by facilitating lysosome fusion²⁸. It is interesting to determine the relationship between LC3 lipidation and acidification of the entotic vacuoles. We therefore established MCF10A cells stably co-expressing keima and EGFP-LC3 and examined the LC3 recruitment to the entotic vacuoles by time-lapse microscopy of 24 h as the first step. As reported, the typical LC3 lipidation, which is rapid, transient and generally occurred within 1 h, of the entotic vacuole were observed right before the entotic death in most of the CICs (53.3%) (Fig. 3A–C and Movie S3). Unexpectedly, a number of vacuoles (40%) also recruited LC3 post inner cell death, which could be subdivided into two classes based on the presence of pre-death LC3 lipidation, i.e., LC3-entosis-LC3 (Fig. 3D) and entosis-LC3 (Fig. 3E and Movie S5). Moreover, we observed two cases of LC3 lipidation that were not associated with any signs of inner cell death in the 24 h duration of time-lapse (Fig. 3F and Movie S6), instead, LC3 either retained for long time (200 min), or was repetitively recruited for multiple times. Furthermore, the post-death LC3 lipidation seemed to be an indispensable event (100%) for the vacuoles that contained cells dying through an apoptotic program (Fig. 3G, H and Movie S4). These findings demonstrated a previously underappreciated relationship between LC3 lipidation and cell death mediated by CICs.

LC3 lipidation associated with vacuolar acidification during the death of internalized cells

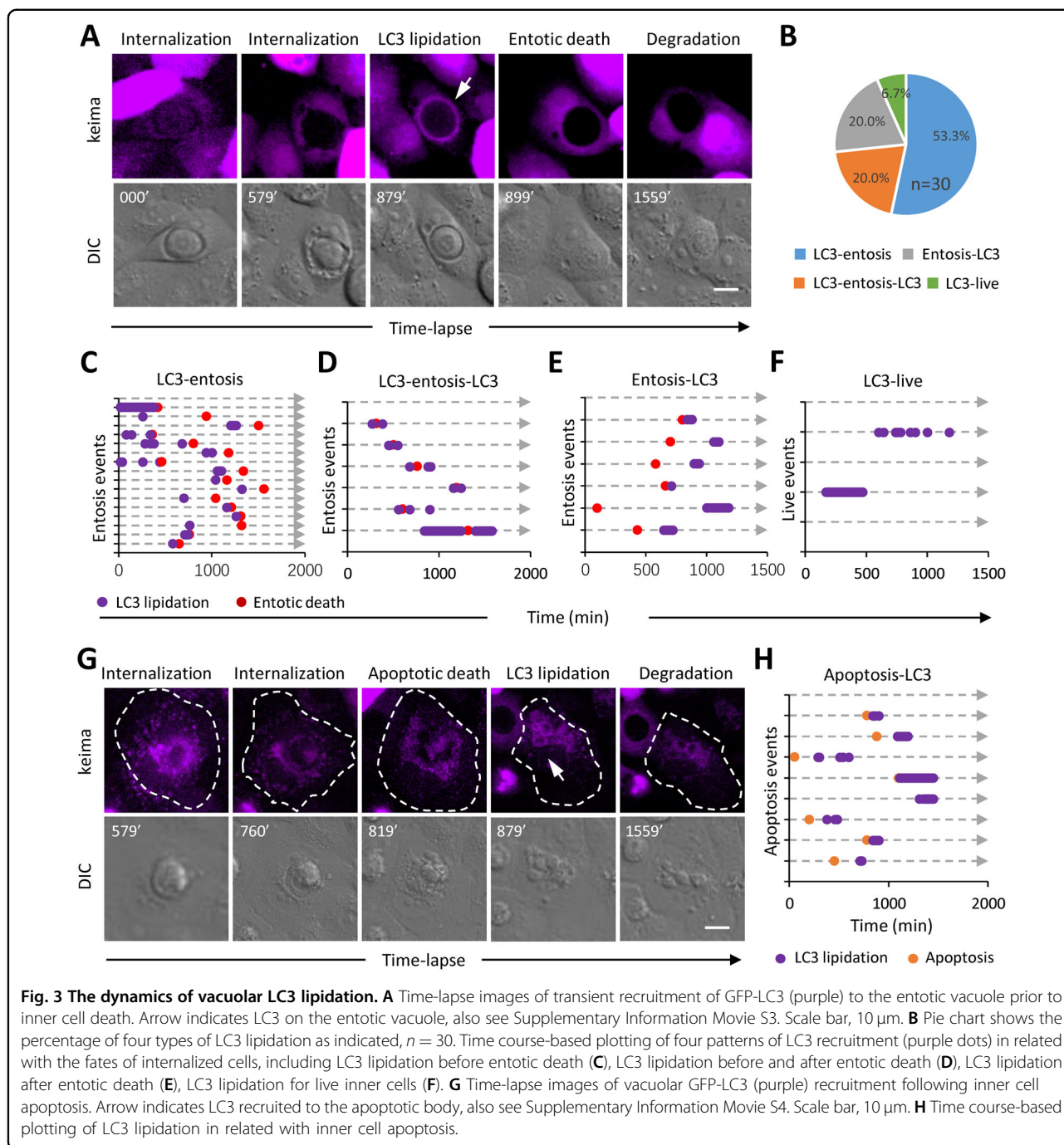
We next investigated the pH change associated with the LC3 lipidation with the co-expressed keima protein. All the pH values associated with the above five patterns of LC3 lipidation were measured in situ and plotted along the time course of death events (Figs. 4C, D and S4A–C,

E, F). For the typical LC3 lipidation that occurred prior to the entotic death of inner cells (Fig. 3A), the pH of entotic vacuoles was in a range of 4.8–6.20 followed by the entotic death of the inner cells at a lower pH about 4.3–5.2 (Fig. 4A, C and Movie S3). By contrast, the apoptotic death of the inner cells took place at a relatively higher pH about 5.3–6.0 followed by LC3 lipidation on the apoptotic bodies at a lower pH about 4.5–5.6 (Fig. 4B, D and Movie S4). And the pH for LC3 lipidation of post-entotic death was about 4.4–4.8, which was frequently preceded by entotic death events of higher pH (4.8–5.6) as compared with that of entotic death without post-death LC3 lipidation (Figs. 4E–G and S4A, B). The pH for LC3 lipidation without death was similar to that of pre-entotic death (Figs. 4G and S4A, C). Nevertheless, all the LC3 lipidation events were followed by a continuous decline of vacuolar pH (Fig. 4H), which is consistent with a role of LC3 lipidation in facilitating entotic vacuoles-lysosome fusion^{28,40}. These data suggested that LC3 lipidation may not occur in responding to a defined range of vacuolar pH, instead, vacuolar acidification was a consequence of LC3 lipidation that not only initiated entotic cell death but also facilitated subsequent degradation of corpses from both entotic and apoptotic death. Consistently, LC3 lipidation took place primarily in entotic vacuoles containing dead cells, either entotic (82.4%) or apoptotic (80.0%), but rather infrequent in vacuoles with live cells (2.4%) (Fig. S4D).

The fate control of internalized cells by vacuolar pH manipulation

Given the pivotal role of pH in determining inner cell death, it is conceivable that manipulating vacuolar acidification might be a way to control inner cell fates. To examine this idea, we first treated MCF10A cells with EN6, an activator of v-ATPase that facilitates vacuolar acidification⁴¹, which significantly lowered the pH of entotic vacuoles containing live cells to around 5.1, a value really close to the range of the death pH (4.0–4.9) (Figs. 2F and 5A). As a result, the death rate of inner cells increased (from ~45 to >65%) (Fig. 5B), and, remarkably, all the death events were exclusively entotic (100%) but not apoptotic (Fig. 5C), as confirmed by immunostaining of cleaved-caspase 3, the marker of apoptosis (Fig. 5D, E). To our best knowledge, this is the first demonstration that enhancing vacuolar acidification could promote CICs-mediated entotic death of internalized cells.

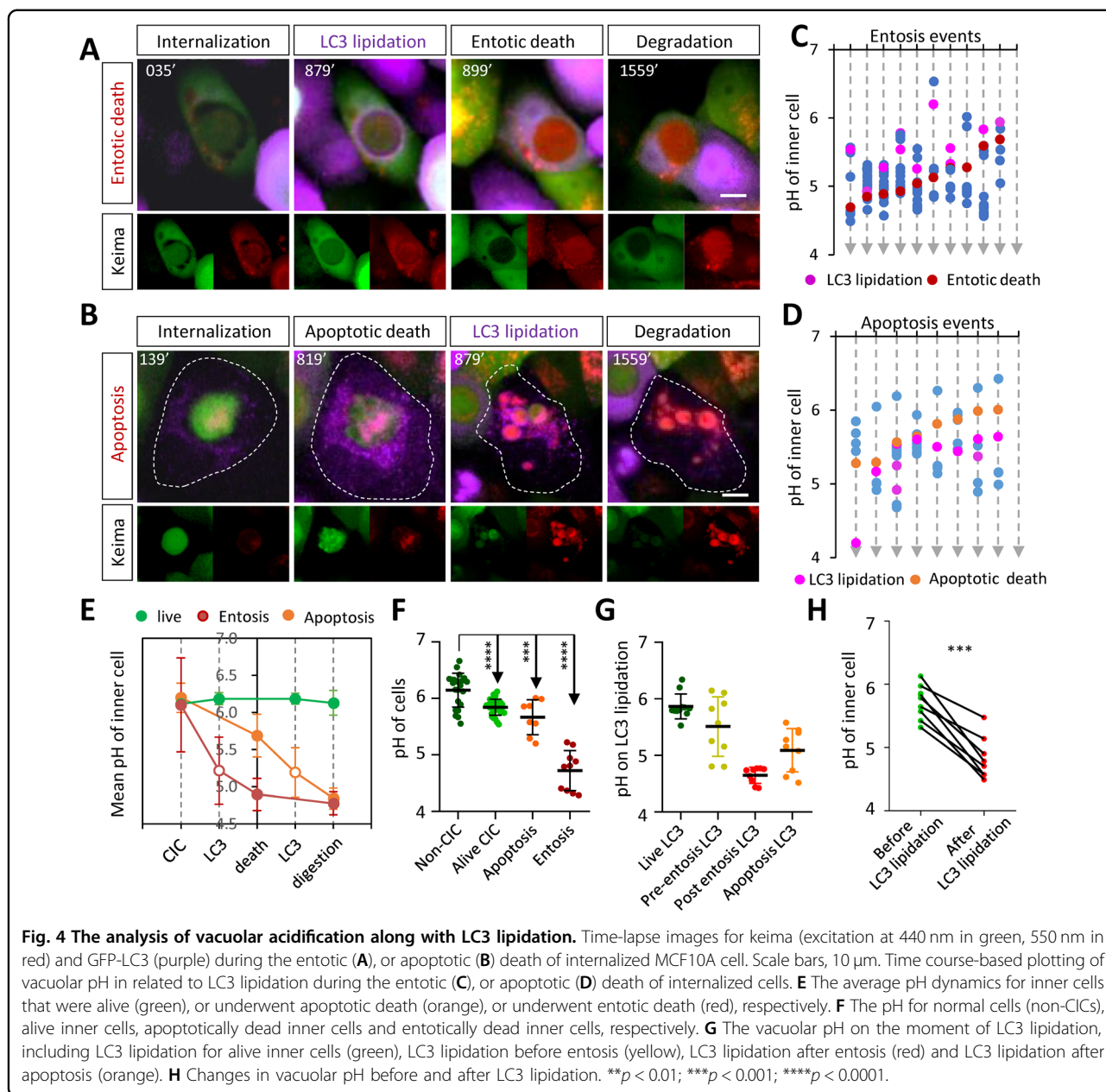
To confirm this finding, we then treated MCF10A cells with compounds that were capable of compromising vacuolar acidification, including ConA that selectively inhibits V-ATPase⁴², chloroquine (CQ) that could inhibit vacuole-lysosome fusion⁴³, and ammonium chloride (NH₄Cl) that could alkalinize intracellular compartments^{44,45}. As expected, the average pH of the entotic



vacuoles containing live cells increased to above 6.1 upon CQ, or ConA, or NH₄Cl treatments (Fig. 5A), leading to much less inner cell death (<30%) as compared with control (>45%) and EN6-treated cells (>65%) (Fig. 5B), and, interestingly, majority of the death were switched to apoptosis (from ~20 to ~80%), and consistent with above observation (Fig. 4C), the mean death pH for apoptosis here is of >5.2 (Fig. 5A). Furthermore, similar results were obtained from the other three CICs-proficient cells,

including MCF7 (Figs. 5F, I and S5), MDA-MB-231 (Fig. 5G, J), and SW480 cells (Fig. 5H, K), and among them, the mean pH of each case was generally higher than that in MCF10A cells (Fig. 5A, F–H).

We next examined the roles of other factors of autophagy pathway in vacuolar pH and entotic death by genetic manipulation. As shown in Fig. S6, knocking down ATG5 or ATG7 (Fig. S6A, B) significantly inhibited LC3 lipidation (Fig. S6C) and raised the pH value of entotic vacuole



containing both dead cell and live cell (Fig. S6D), partially rescued inner cells from death (Fig. S6E), and mostly converted entotic death to apoptosis (Fig. S6F). These data suggested that the autophagy machineries upstream of LC3 lipidation were involved in vacuolar acidification and entotic death of inner cells. Furthermore, knocking down ATP6V0A2 and ATP6V1A (Fig. S6G), two critical components of V-ATPase complex, impacted vacuolar acidification and entotic cell death in a way resembling that of treatment with ConA (Figs. 5A–C and S6H–J), a selective inhibitor of V-ATPase. Together, these results support that the inner cell death of a CIC structure was dictated by the vacuolar pH and could be manipulated

genetically by interference RNAs and biochemically by compounds that regulate the acidification of intracellular vacuoles.

Discussion

We studied the dynamic process of pH change in the internalized cells in the CICs by keima, a fluorescent protein pH meter. We determined the lysosome-dependent death pH critical for the entotic death (Fig. 6), and identified LC3 lipidation onto the entotic vacuole as a preceding condition for the pH declining to a critical value and evoke the entotic death. Meanwhile, the LC3 lipidation following cell death, primarily apoptotic and, to a lesser extends, entotic, would

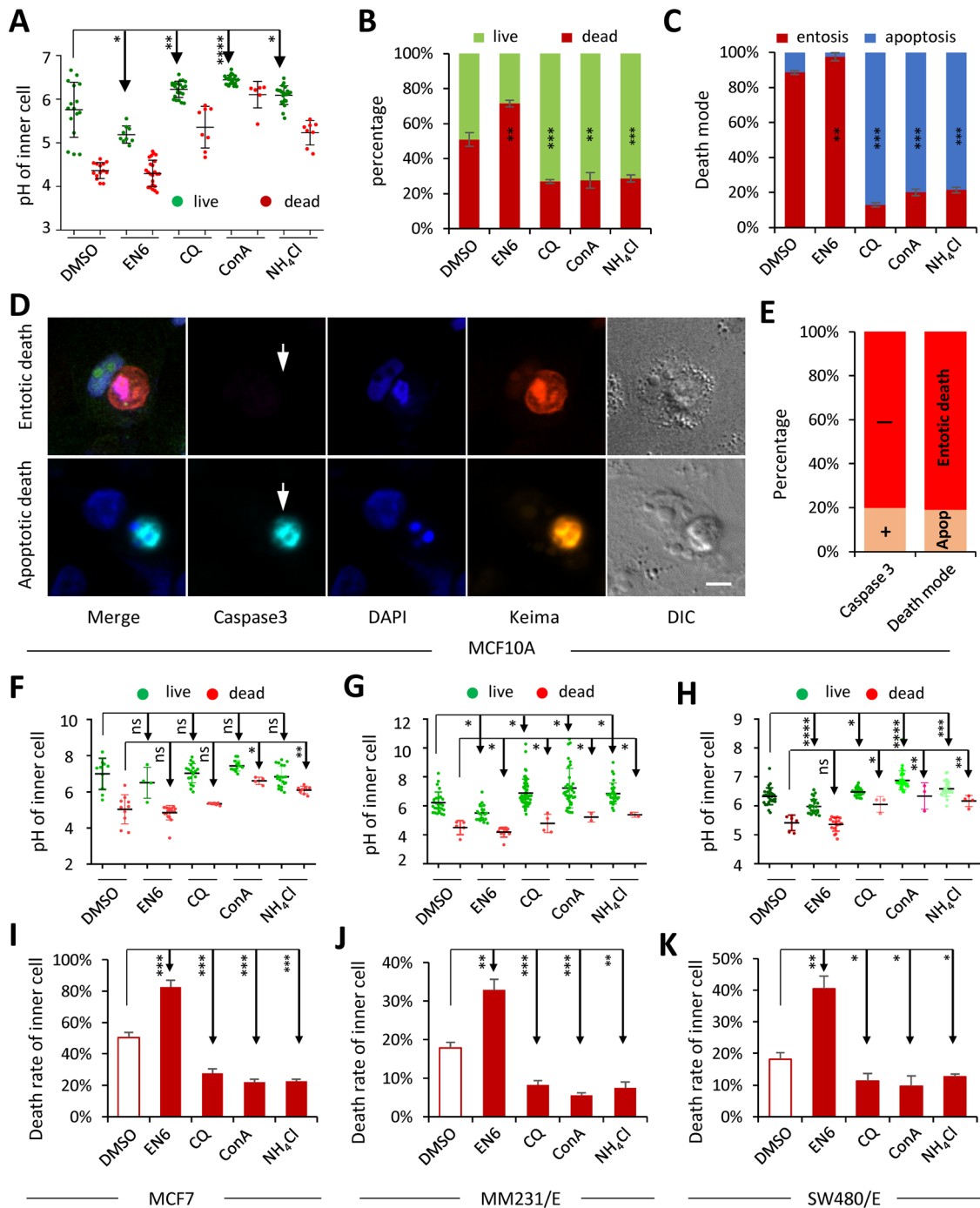
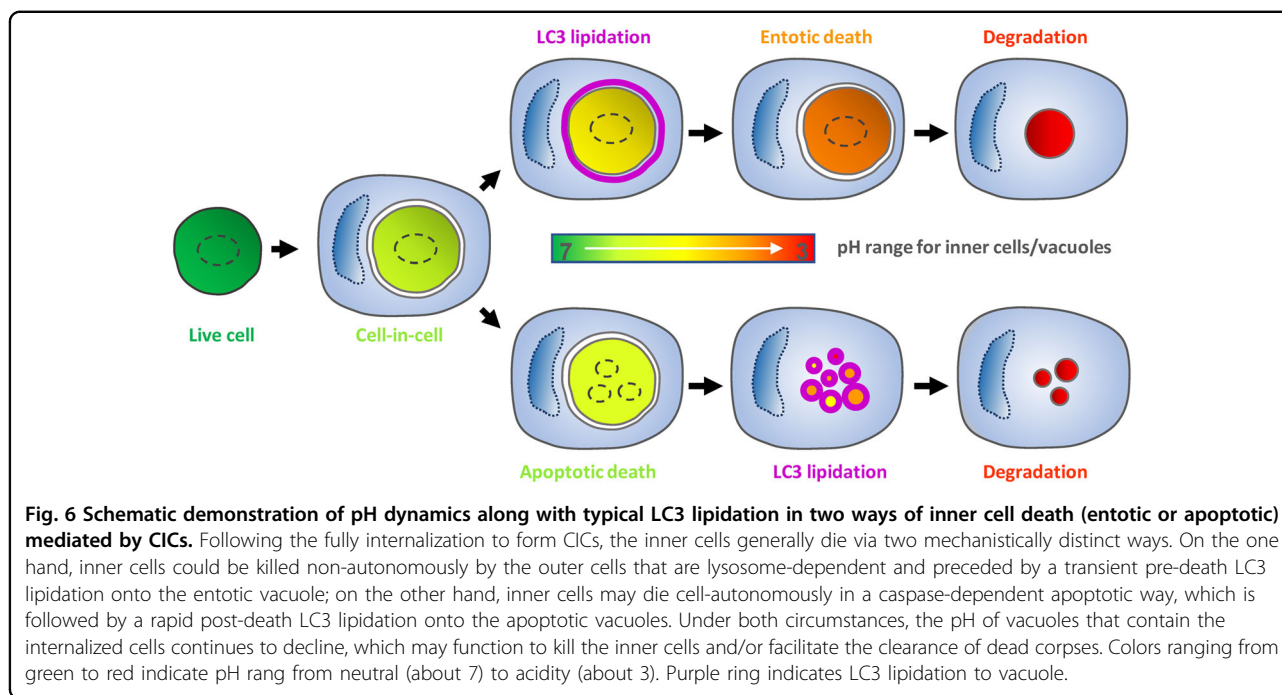


Fig. 5 The fates of inner cells were controlled by vacuolar pH. The pH of vacuoles containing live or dead inner cells (A), and inner cell fates (B), and the ways inner cells died (entotic or apoptotic) (C), for MCF10A cells upon treatments with EN6 (10 μM), CQ (20 μM), ConA (200 nM), and NH₄Cl (100 μM). *n* (left to right) = 30, 33, 30, 31, 30 for A; 96, 98, 89, 94, 104 for B; 150, 129, 76, 65, 60 for C. ***p* < 0.01; ****p* < 0.001. D Representative images of CICs, with inner cells undergoing entotic death (up) or apoptotic death (low), that were stained with antibody for cleaved-caspase 3 (cyan). Keima for merged channels of 440 and 550 nm. White arrows indicate inner cells. Scale bar, 10 μm. E Quantification of inner cells that were positive in cleaved-caspase 3, or died either entotically or apoptotically. *n* (left to right) = 64, 57, respectively. The pH of vacuoles containing live or dead inner cells (F–H), and inner cell fates (I–K), for cells (MCF7, MM231/E, and SW480/E) upon treatments with EN6 (10 μM), CQ (20 μM), ConA (200 nM), and NH₄Cl (100 μM), respectively. *n* (left to right) = 26, 23, 26, 20, 28 for F; 31, 32, 57, 38, 33 for G; 36, 43, 32, 37, 32 for H; 89, 78, 96, 80, 85 for I; 117, 118, 159, 160, 108 for J; 120, 108, 104, 134, 141 for K. **p* < 0.05; ***p* < 0.01; ****p* < 0.001; *****p* < 0.0001.



promote the clearance of dead corpse by facilitating vacuolar acidification.

It is known that fluorescent dyes, such as LysoTracker, could efficiently label acidified intracellular vacuoles and emit bright signals, and were generally employed to detect acidified vacuoles³⁹. However, these dyes, due to strong phototoxicity and easily to be quenched, were not good candidates for long period of time-lapse imaging, particular for the process of CIC-mediated death that usually takes place within a period of up to >10 h. Whereas the fluorescent proteins, such as keima, were ideal alternatives attributed to their properties of optional excitation spectra and ratio-based measurement⁴⁶. As a proof of concept for the application in CIC-mediated death, we chose four entosis-proficient cell lines, and examined the feasibility of keima as a pH meter to probe the role and dynamics of vacuolar acidification along with the inner cell death by long period (~24 h) of time-lapse microscopy, which reported ideal results. Meanwhile, our study uncovered a number of previously unrecognized findings in terms of pH changes during CIC-mediated death, which set a basis for further investigation.

It is worth to point out that the pH of cells was correlated to the pH of lysosome in these four cell lines. The cytoplasmic pH and lysosomal pH of the MCF7 cells were the highest whereas those of the MDA-MB-231 cells were the lowest (Fig. S1B, C). Moreover, we found that lysosome pH and cellular pH were both positively related to entotic death rate for these four cell lines (Fig. S1B–D), suggesting that the cellular or even environmental pH might have profound impacts on cells' behaviors. Indeed,

there were studies showing that cancer cells were actually grown in acidic tumor microenvironment^{47,48}, under which circumstance, MDA-MB-231 cells displayed high metastatic potentials than did MCF7 cells⁴⁹, consistent with the idea that the cytoplasmic pH and lysosomal pH were somehow related to the metastasis and malignancy of the tumor cells.

Interestingly, in addition to a clear role of vacuolar pH in dictating inner cell fates and the ways whereby inner cells die, complicated relationships were observed among the pH titration behaviors of the four cell lines (Fig. 1B–E). For instances, the cellular pH and the lysosomal pH were positively correlated to entotic death time for MCF10A, SW480, MDA-MB-231 cell lines but not for MCF7 cell line (Figs. S1B, C and S2C); the rate of pH change was correlated to the death rate of the inner cells for MCF7, MCF10A, SW480 cell lines but not for MDA-MB-231 cell line (Figs. S1D and S2A); despite of the negative correlation between the rate of pH change and the death time of the inner cells (Fig. S2D–G), there was no correlation between the death pH and the lysosome pH (Figs. S1B and S2B). The above complicated relationships might be due to the significant genotypic and proteomic differences among these cell lines, or were related to the cell metabolism regulated by lysosome as reported^{50,51}.

As our results suggested that vacuolar pH levels were not a trigger, but a consequence instead, of LC3 lipidation onto the entotic vacuoles, and an interesting issue, though might be beyond the scope of this study, is what are the upstream factors that dictate the initiation of LC3

lipidation. Though the LC3 lipidation was executed in the outer cells, the commanding signals were likely from the internalized cells as the apoptosis of inner cells seemed to be always followed shortly by the LC3 lipidation. Actually, previous study indicated that osmotic changes in the vacuoles could efficiently induce LC3 lipidation, which required activity of the vacuolar-type H (+)-ATPase (V-ATPase)⁴². Thus, it is conceivable that LC3 lipidation followed the entotic death might be a result of increased osmotic changes in the vacuoles, which ended up with increased vacuolar pH that facilitates the degradation and clearance of the dead corpse. Since CIC structures in tumor cells were believed to promote cell competition, clonal selection and tumor evolution by multiple mechanisms, such as conferring growth advantages to the outer survivors via consuming the dead inner cells^{1,9}, interfering with the vacuolar acidification might be a potential strategy for the treatment of cancers undergoing active CIC formation.

Acknowledgements

We thank Dr. Songzhi Gu for microscope operation.

Funding

This work was supported by the National Key Research and Development Program of China (2019YFA0903801 and 2018YFA0900804), the National Natural Science Foundation of China (31970685, 31671432, and 81872314), the Fundamental Research Funds for the Central Universities (WK2480000006) and Anhui Province Science and Technology Major Project (201903a07020019).

Author details

¹CAS Key Laboratory of Mechanical Behavior and Design of Materials, Department of Modern Mechanics, University of Science and Technology of China, Hefei, China. ²Laboratory of Cell Engineering, Institute of Biotechnology, Beijing, China. ³Department of Oncology, Beijing Shijitan Hospital of Capital Medical University, Beijing, China. ⁴College of Life Science and Bioengineering, School of Science, Beijing Jiaotong University, Beijing, China. ⁵Research Unit of Cell Death Mechanism, 2020RU009, Chinese Academy of Medical Science, Beijing, China

Author contributions

Concept and design: Q.S.; phenotype: Y.S.; gene cloning: H.R. and B.Z.; data collection: Y.S., H.R., X.H., Z.N., and L.G.; figures: Y.S., Q.S., T.L., M.T., X.G., and Y.Z.; data interpretation: Q.S., T.L., and Y.S.; manuscript: Q.S., T.L., and Y.S., with input from M.T., Y.Z., Z.N., Z.W., H.J., C.W., and H.R.; funding: Q.S., Y.Z., Z.C., and T.L. All authors have read and approved the final manuscript.

Conflict of interest

The authors declare that they have no conflict of interest.

Ethical approval

This study did not involve ethical approval.

Publisher's note

Springer Nature remains neutral with regard to jurisdictional claims in published maps and institutional affiliations.

Supplementary Information The online version contains supplementary material available at (<https://doi.org/10.1038/s41419-021-03396-2>).

Received: 13 October 2020 Revised: 14 December 2020 Accepted: 16 December 2020

Published online: 22 January 2021

References

- Huang, H., Chen, Z. & Sun, Q. Mammalian cell competitions, cell-in-cell phenomena and their biomedical implications. *Curr. Mol. Med.* **15**, 852–860 (2015).
- Fais, S. & Overholtzer, M. Cell-in-cell phenomena in cancer. *Nat. Rev. Cancer* **18**, 758–766 (2018).
- Cano, C. E. et al. Homotypic cell cannibalism, a cell-death process regulated by the nuclear protein 1, opposes to metastasis in pancreatic cancer. *EMBO Mol. Med.* **4**, 964–979 (2012).
- Huang, H. et al. Identification and validation of heterotypic cell-in-cell structure as an adverse prognostic predictor for young patients of resectable pancreatic ductal adenocarcinoma. *Signal Transduct. Target Ther.* **5**, 246 (2020).
- Schenker, H., Büttner-Herold, M., Fietkau, R. & Distel, L. V. Cell-in-cell structures are more potent predictors of outcome than senescence or apoptosis in head and neck squamous cell carcinomas. *Radiat. Oncol.* **12**, 21 (2017).
- Fan, J. et al. Role of heterotypic neutrophil-in-tumor structure in the prognosis of patients with buccal mucosa squamous cell carcinoma. *Front. Oncol.* **10**, 541878 (2020).
- Zhang, X. et al. Subtype-based prognostic analysis of cell-in-cell structures in early breast cancer. *Front. Oncol.* **9**, 895 (2019).
- Ruan, B. et al. High frequency of cell-in-cell formation in heterogeneous human breast cancer tissue in a patient with poor prognosis: a case report and literature review. *Front. Oncol.* **9**, 1444 (2019).
- Sun, Q. et al. Competition between human cells by entosis. *Cell Res.* **24**, 1299–1310 (2014).
- Lee, Y. et al. Entosis controls a developmental cell clearance in *C. elegans*. *Cell Rep.* **26**, 3212–3220.e3214 (2019).
- Mackay, H. L. et al. Genomic instability in mutant p53 cancer cells upon entotic engulfment. *Nat. Commun.* **9**, 3070 (2018).
- Liang, J. et al. p53-dependent elimination of aneuploid mitotic offspring by entosis. *Cell Death Differ.* <https://doi.org/10.1038/s41418-020-00645-3> (2020).
- Ni, C. et al. Implication of cell-in-cell structures in the transmission of HIV to epithelial cells. *Cell Res.* **25**, 1265–1268 (2015).
- Ni, C. et al. In-cell infection: a novel pathway for Epstein-Barr virus infection mediated by cell-in-cell structures. *Cell Res.* **25**, 785–800 (2015).
- Davies, S. P. et al. Hepatocytes delete regulatory T cells by encyclus, a CD4(+) T cell engulfment process. *Cell Rep.* **29**, 1610–1620.e1614 (2019).
- Benseler, V. et al. Hepatocyte entry leads to degradation of autoreactive CD8 T cells. *Proc. Natl Acad. Sci. USA* **108**, 16735–16740 (2011).
- Ning, X., Luo, T., Chen, Z. & Sun, Q. The physics for the formation of cell-in-cell structures. *Curr. Mol. Med.* **15**, 867–872 (2015).
- Sun, Q., Cibas, E. S., Huang, H., Hodgson, L. & Overholtzer, M. Induction of entosis by epithelial cadherin expression. *Cell Res.* **24**, 1288–1298 (2014).
- Wang, M. et al. Mechanical ring interfaces between adherens junction and contractile actomyosin to coordinate entotic cell-in-cell formation. *Cell Rep.* **32**, 108071 (2020).
- Hinojosa, L. S., Holst, M., Baarlink, C. & Grosse, R. MRTF transcription and Ezzin-dependent plasma membrane blebbing are required for entotic invasion. *J. Cell Biol.* **216**, 3087–3095 (2017).
- Purvanov, V., Holst, M., Khan, J., Baarlink, C. & Grosse, R. G-protein-coupled receptor signaling and polarized actin dynamics drive cell-in-cell invasion. *Elife* **3**. <https://doi.org/10.7554/eLife.02786> (2014).
- Wang, C. et al. PCDH7 inhibits the formation of homotypic cell-in-cell structure. *Front. Cell Dev. Biol.* **8**, 329 (2020).
- Ruan, B. et al. Cholesterol inhibits entotic cell-in-cell formation and actomyosin contraction. *Biochem. Biophys. Res. Commun.* **495**, 1440–1446 (2018).
- Ruan, B. et al. Expression profiling identified IL-8 as a regulator of homotypic cell-in-cell formation. *BMB Rep.* **51**, 412–417 (2018).
- Liang, J. et al. CDKN2A inhibits formation of homotypic cell-in-cell structures. *Oncogenesis* **7**, 50 (2018).
- Martins, I. et al. Entosis: the emerging face of non-cell-autonomous type IV programmed death. *Biomed. J.* **40**, 133–140 (2017).
- Overholtzer, M. et al. A nonapoptotic cell death process, entosis, that occurs by cell-in-cell invasion. *Cell* **131**, 966–979 (2007).
- Florey, O., Kim, S. E., Sandoval, C. P., Haynes, C. M. & Overholtzer, M. Autophagy machinery mediates macroendocytic processing and entotic cell death by targeting single membranes. *Nat. Cell Biol.* **13**, 1335–1343 (2011).

29. Krajcovic, M., Krishna, S., Akkari, L., Joyce, J. A. & Overholtzer, M. mTOR regulates phagosome and entotic vacuole fission. *Mol. Biol. Cell* **24**, 3736–3745 (2013).
30. Krishna, S. et al. PIKfyve regulates vacuole maturation and nutrient recovery following engulfment. *Dev. Cell* **38**, 536–547 (2016).
31. Miesenböck, G., De Angelis, D. A. & Rothman, J. E. Visualizing secretion and synaptic transmission with pH-sensitive green fluorescent proteins. *Nature* **394**, 192–195 (1998).
32. Violot, S., Carpentier, P., Blanchoin, L. & Bourgeois, D. Reverse pH-dependence of chromophore protonation explains the large Stokes shift of the red fluorescent protein mKeima. *J. Am. Chem. Soc.* **131**, 10356–10357 (2009).
33. Katayama, H., Kogure, T., Mizushima, N., Yoshimori, T. & Miyawaki, A. A sensitive and quantitative technique for detecting autophagic events based on lysosomal delivery. *Chem. Biol.* **18**, 1042–1052 (2011).
34. Lindqvist, L. M. et al. Autophagy induced during apoptosis degrades mitochondria and inhibits type I interferon secretion. *Cell Death Differ.* **25**, 784–796 (2018).
35. Nguyen, T. N. et al. Atg8 family LC3/GABARAP proteins are crucial for autophagosome-lysosome fusion but not autophagosome formation during PINK1/Parkin mitophagy and starvation. *J. Cell Biol.* **215**, 857–874 (2016).
36. Ponimaskin, E. G., Profirovic, J., Vaiskunaitė, R., Richter, D. W. & Voyno-Yasnetskaya, T. A. 5-Hydroxytryptamine 4(a) receptor is coupled to the Galpha subunit of heterotrimeric G13 protein. *J. Biol. Chem.* **277**, 20812–20819 (2002).
37. Zhang, Z. et al. Acidic pH environment induces autophagy in osteoblasts. *Sci. Rep.* **7**, 46161 (2017).
38. Sun, Q. & Overholtzer, M. Methods for the study of entosis. *Methods Mol. Biol.* **1004**, 59–66 (2013).
39. Chikte, S., Panchal, N. & Warnes, G. Use of LysoTracker dyes: a flow cytometric study of autophagy. *Cytom. A* **85**, 169–178 (2014).
40. Lai, S. C. & Devenish, R. J. LC3-associated phagocytosis (LAP): connections with host autophagy. *Cells* **1**, 396–408 (2012).
41. Chung, C. Y. et al. Covalent targeting of the vacuolar H(+)-ATPase activates autophagy via mTORC1 inhibition. *Nat. Chem. Biol.* **15**, 776–785 (2019).
42. Florey, O., Gammoh, N., Kim, S. E., Jiang, X. & Overholtzer, M. V-ATPase and osmotic imbalances activate endolysosomal LC3 lipidation. *Autophagy* **11**, 88–99 (2015).
43. Mauthe, M. et al. Chloroquine inhibits autophagic flux by decreasing autophagosome-lysosome fusion. *Autophagy* **14**, 1435–1455 (2018).
44. Dabydeen, S. A. & Meneses, P. I. The role of NH₄Cl and cysteine proteases in Human Papillomavirus type 16 infection. *Virology* **6**, 109 (2009).
45. Kim, Y. Y. et al. Assessment of mitophagy in mt-Keima Drosophila revealed an essential role of the PINK1-Parkin pathway in mitophagy induction in vivo. *FASEB J.* **33**, 9742–9751 (2019).
46. Sun, N. et al. A fluorescence-based imaging method to measure in vitro and in vivo mitophagy using mt-Keima. *Nat. Protoc.* **12**, 1576–1587 (2017).
47. Roma-Rodrigues, C., Mendes, R., Baptista, P. V. & Fernandes, A. R. Targeting tumor microenvironment for cancer therapy. *Int. J. Mol. Sci.* **20**. <https://doi.org/10.3390/ijms20040840> (2019).
48. Wojtkowiak, J. W., Verduzco, D., Schramm, K. J. & Gillies, R. J. Drug resistance and cellular adaptation to tumor acidic pH microenvironment. *Mol. Pharm.* **8**, 2032–2038 (2011).
49. Aumsuwan, P., Khan, S. I., Khan, I. A., Walker, L. A. & Dasmahapatra, A. K. Gene expression profiling and pathway analysis data in MCF-7 and MDA-MB-231 human breast cancer cell lines treated with dioscin. *Data Brief.* **8**, 272–279 (2016).
50. Settembre, C., Fraldi, A., Medina, D. L. & Ballabio, A. Signals from the lysosome: a control centre for cellular clearance and energy metabolism. *Nat. Rev. Mol. Cell Biol.* **14**, 283–296 (2013).
51. Dubland, J. A. & Francis, G. A. Lysosomal acid lipase: at the crossroads of normal and atherogenic cholesterol metabolism. *Front. Cell Dev. Biol.* **3**, 3 (2015).